

1 **Diurnal variations of NO<sub>2</sub> tropospheric vertical column density over the Seoul**  
2 **Metropolitan Area from the Geostationary Environment Monitoring**  
3 **Spectrometer (GEMS): seasonal differences and the influence of the *a priori* NO<sub>2</sub>**  
4 **profile**

5

6 Seunghwan Seo<sup>1</sup>, Si-Wan Kim<sup>1,2\*</sup>, Kyoung-Min Kim<sup>1</sup>, Andreas Richter<sup>3</sup>, Kezia Lange<sup>3</sup>,  
7 John P. Burrows<sup>3</sup>, Junsung Park<sup>4\*\*</sup>, Hyunkee Hong<sup>5</sup>, Hanlim Lee<sup>4</sup>, Ukkyo Jeong<sup>4</sup>, Jung-  
8 Hun Woo<sup>6\*\*\*</sup>, and Jhoon Kim<sup>1\*</sup>

9

10 <sup>1</sup>Department of Atmospheric Sciences, Yonsei University, Seoul, Republic of Korea

11 <sup>2</sup>Irreversible Climate Change Research Center, Yonsei University, Seoul, Republic of  
12 Korea

13 <sup>3</sup>Institute of Environmental Physics, University of Bremen, Bremen, Germany

14 <sup>4</sup>Division of Earth Environmental System Science, Major of Spatial Information  
15 Engineering, Pukyong National University, Busan, Republic of Korea

16 <sup>5</sup>National Institute of Environmental Research, Incheon, Republic of Korea

17 <sup>6</sup>Department of Technology Fusion Engineering, College of Engineering, Konkuk  
18 University, Seoul, Republic of Korea

19

20 \*To whom correspondence should be addressed:

21 Si-Wan Kim (e-mail: [siwan.kim@yonsei.ac.kr](mailto:siwan.kim@yonsei.ac.kr)) and Jhoon Kim (e-mail:  
22 [jkim2@yonsei.ac.kr](mailto:jkim2@yonsei.ac.kr)).

23 \*\* now at: Center for Astrophysics | Harvard & Smithsonian, Cambridge, MA, USA

1 \*\*\*now at: Graduate School of Environmental Studies, Seoul National University, Seoul,

2 Republic of Korea

3 Date: 10/13/2024

4

## 1 **Abstract**

2 The Geostationary Environment Monitoring Spectrometer (GEMS), launched in 2020,  
3 provides both temporally and spatially continuous air quality data from geostationary  
4 Earth orbit (GEO). This study first investigates the seasonal variations and diurnal  
5 behavior of nitrogen dioxide (NO<sub>2</sub>) tropospheric vertical column densities (TropVCDs)  
6 over the Seoul Metropolitan Area (SMA) using GEMS data, retrieved by the IUP-UB  
7 algorithm. We find that the magnitude of the NO<sub>2</sub> TropVCDs and its diurnal behavior  
8 have significant seasonal dependences. In January, the highest NO<sub>2</sub> TropVCD values in  
9 the range  $27.5 - 28.9 \times 10^{15}$  molec. cm<sup>-2</sup> during the four seasons were observed at 15:00  
10 local time (LT), and NO<sub>2</sub> TropVCD increases from the first retrieved values at 10:00  
11 LT. On the other hand, we find the lowest values ( $7.4 - 8.8 \times 10^{15}$  molec. cm<sup>-2</sup>) are at  
12 ~14:00 LT in July. The VCD values in July increased up to 10:00 LT, then decreased  
13 until 14:00 LT, but then began to increase again. These different diurnal behaviors of  
14 the TropVCDs in the different seasons reflect the differences in photochemical and  
15 meteorological conditions as well as the emissions of NO<sub>x</sub>. Photochemical  
16 transformations are typically more rapid in July and slower in January. The absolute  
17 values and diurnal behavior of NO<sub>2</sub> TropVCDs are significantly influenced by the wind  
18 speed, except in July. Moderate (wind speed  $\geq 3$  m/s) or strong wind (wind speed  $> 5$  m/s)  
19 reduced the magnitude of the diurnal behavior in January, implying that the NO<sub>2</sub> plumes  
20 were transported downwind. Finally, we investigate the retrieved NO<sub>2</sub> TropVCDs with  
21 that retrieved using different *a priori* NO<sub>2</sub> data simulated by TM5 and WRF-Chem,  
22 calculated using the most recent emission inventories. Although simulated VCDs from  
23 WRF-Chem and TM5 show differences of up to a factor 2.75, retrieved NO<sub>2</sub> TropVCDs  
24 using each *a priori* data have almost identical values and diurnal behaviors, except in  
25 July. Notably, the diurnal behavior of the retrieved NO<sub>2</sub> TropVCDs are independent of  
26 those from the two chemical transport models, indicating that observations of slant  
27 column densities are the dominant factor in determining the diurnal behavior of NO<sub>2</sub>  
28 TropVCDs. Changes of the model horizontal resolution and volatile organic compounds  
29 (VOC) emission inventory do not affect significantly the retrieved NO<sub>2</sub> TropVCDs in

1 this study. However, when the *a priori* NO<sub>2</sub> vertical profile was fixed as the values at  
2 13:45 LT, the diurnal patterns of NO<sub>2</sub> TropVCDs showed significant changes with  
3 differences of up to -18.3%.

## 1 **1. Introduction**

2 Nitrogen dioxide (NO<sub>2</sub>) is one of the most important trace gases in the photochemical  
3 mechanisms, which determine the tropospheric distributions of ozone and secondary  
4 aerosol (Milford et al., 1989). Beginning with the launch of the passive remote sensing  
5 instrument GOME on ESA ERS-2 (Burrows et al., 1999) in 1995, then followed by  
6 SCIAMACHY on ESA Envisat in 2002 (Burrows et al., 1995 and Bovensmann et al.,  
7 1999), OMI on NASA AURA (Levelt et al., 2006), GOME-2 on ESA EUMETSAT  
8 Metop A, B and C (Callies et al., 2000, Munro et al., 2016), and TROPOMI on the ESA  
9 Sentinel 5 Precursor in 2018 (Veefkind et al., 2012), the amounts and distributions of  
10 stratospheric and tropospheric NO<sub>2</sub> vertical column densities (TropVCDs) have been  
11 retrieved at increasing spatial resolutions from these instruments, which all fly in sun-  
12 synchronous low earth orbit (LEO). By using the retrieved NO<sub>2</sub> TropVCDs from the  
13 LEO instruments, the tropospheric nitrogen oxide sources have been identified and their  
14 NO<sub>x</sub> emissions have been estimated, and the chemistry of the troposphere has been  
15 studied from the local to the global scale. While instruments on board LEO satellites  
16 provide spatially continuous data, observations are obtained only once or twice per day.  
17 It was recognized in the late 1990s that instruments similar to SCIAMACHY in  
18 geostationary orbit (GEO) would potentially deliver the diurnal variations of key trace  
19 gases (see the GeoTROPE concept in Burrows et al., 2004 and references therein). The  
20 measurements at the top of the atmosphere of the Geostationary Environment  
21 Monitoring Spectrometer (GEMS), launched in 2020, yield the first not only spatially  
22 but also temporally continuous air quality data over Asia from the geostationary orbit  
23 GEO (see Kim et al., 2020).

24 Mathematical inversion of the GEMS observations provides diurnal variations  
25 of the NO<sub>2</sub> TropVCD. These data products enable the seasonal changes not only in  
26 pollutant concentration but also in temporal characteristics, such as the times of the  
27 maxima and minima and the sources and sinks of NO<sub>2</sub>, which vary by diurnally and

1 seasonally, to be studied for the first time from space.

2           As part of the differential optical absorption spectroscopy (DOAS) retrieval of  
3 NO<sub>2</sub> TropVCD data, air mass factors (AMF) are used to convert slant column density  
4 (SCD) to VCD. The assumptions used in the AMF calculation are explained in  
5 Richter and Burrows (2002) and Palmer et al (2001). In agreement with other studies,  
6 Lorente et al. (2017) reported that the AMF calculation is the largest source of error or  
7 uncertainty in NO<sub>2</sub> satellite retrievals. This is because of the assumption used to  
8 determine the ancillary or prior data used in the AMF calculation, such as surface albedo,  
9 terrain height, cloud parameters, and trace gas profiles. Consequently, the selection of  
10 optimal and appropriate *a priori* data is essential to accurately retrieve NO<sub>2</sub> TropVCDs  
11 from the observations of any nadir-sounding satellite spectrometer. This is in addition  
12 to the need to separate upper atmospheric NO<sub>2</sub> from that in the troposphere.

13           In this study we investigate two important issues using the GEMS NO<sub>2</sub>  
14 TropVCD data over the Seoul Metropolitan Area (SMA): (1) the influence of *a priori*  
15 profiles on the retrieved GEMS NO<sub>2</sub> TropVCDs and (2) the seasonal variation of the  
16 GEMS NO<sub>2</sub> TropVCD. In section 2 we describe the methods and data used.

17           Prior to our geophysical interpretation of the NO<sub>2</sub> TropVCD, in Section 3 we  
18 compared three GEMS datasets, retrieved with different *a priori* data from the WRF-  
19 Chem model. Thereby we investigated the influence of the inventories of the emissions  
20 of NO<sub>x</sub>, defined as the sum of nitrogen monoxide (NO) and nitrogen dioxide (NO<sub>2</sub>) in  
21 an air mass, on the simulated and retrieved NO<sub>2</sub> TropVCD.

22           In Section 4, we utilized two chemical transport models (CTM), the Weather  
23 Research and Forecast model combined with Chemistry (WRF-Chem) and the global  
24 chemistry transport model TM5 (Tracer Model 5) to analyze both the seasonal  
25 variations and the influence of *a priori* NO<sub>2</sub> profiles. The seasonal changes in the  
26 magnitudes and the time of the maxima of the diurnal NO<sub>2</sub> TropVCD, which we define  
27 as the peak times, were investigated. The differences in the spatial distributions of NO<sub>2</sub>

1 TropVCD between the WRF-Chem- and TM5-based GEMS datasets using different *a*  
2 *priori* data, were identified for each season and peak time. We also analyzed the  
3 influence of wind speed on the variations in the magnitude and diurnal behavior of the  
4 retrieved NO<sub>2</sub> TropVCDs.

5

6 **2. Data and methods**

7 **2.1. GEMS products**

8 GEMS is an ultraviolet-visible (UV-VIS) instrument, measuring contiguously the  
9 spectral range from 300 to 500 nm at a spectral resolution of ~ 0.6 nm (Kim et al.,  
10 2020). The nominal spatial resolution is 3.5 km × 7.7 km for gases including NO<sub>2</sub> data  
11 products. The overall field of regard (FOR) of GEMS covers 75° – 145°E longitude and  
12 5°S – 45°N latitude. GEMS measures hourly during the daytime. The number of  
13 observations varies depending on the month, as a result of the length of the day and the  
14 measurement strategy. For South Korea, observations are least frequent in January, with  
15 six observations per day, and most frequent from April to September, with ten  
16 observations per day. We utilized GEMS NO<sub>2</sub> TropVCD data with the IUP-UB  
17 algorithm (GEMS IUP-UB products) in January, April, July, and October 2021 –  
18 detailed explanations of GEMS IUP-UB products are shown in Section 2.1.1.

19

20 **2.1.1. GEMS IUP-UB products v1.0**

21 The GEMS NO<sub>2</sub> vertical columns used in this study are from the scientific data product  
22 of the University of Bremen, version 1.0 (Lange et al., 2024, Richter et al., *in*  
23 *preparation*). NO<sub>2</sub> slant columns are retrieved in the large fitting window 405 – 485nm  
24 to reduce noise. In addition to the cross-sections of other absorbing species (O<sub>3</sub>, O<sub>4</sub>,  
25 H<sub>2</sub>O and liquid water) pseudo cross-sections for the Ring effect, for GEMS instrument  
26 polarization sensitivity and the effects of scene inhomogeneity are included. The

1 stratospheric correction is performed using the STRatospheric Estimation Algorithm  
2 from Mainz (STREAM) (Beirle et al., 2016). Conversion to vertical tropospheric  
3 columns is based on look-up tables of altitude dependent air mass factors calculated  
4 with the radiative transfer model SCIATRAN (Rozanov et al., 2014) using Lambertian  
5 equivalent reflectivity (LER) surface reflection values from the TROPOMI climatology  
6 (Tilstra et al., 2023). To apply the cloud correction, adjusted cloud fractions and  
7 pressure from the GEMS L2 cloud product were used. Further information about IUP-  
8 UB products is described in Richter et al. (*in preparation*). The NO<sub>2</sub> *a priori* data are  
9 different in the different model simulations, which we call runs, as explained below.

10

## 11 **2.2. Experiment designs**

12 To analyze the spatiotemporal characteristics of GEMS NO<sub>2</sub> VCDs and the impacts of  
13 different *a priori* data on the retrieved values, we undertook five experiments, called  
14 TM5, CTRL, CONST, FINE, and MIXED.

15 The TM5 experiment applies the standard GEMS IUP-UB products v1.0,  
16 which use the TM5 model, as their *a priori* data (Huijnen et al., 2010, Williams et al.,  
17 2017). The meteorological data for TM5 simulations are obtained from the European  
18 Centre for Medium-Range Weather Forecasts (ECMWF) operational forecast data. For  
19 the anthropogenic NO<sub>x</sub> emission inventory of TM5, the MACCity emission estimates  
20 are adopted (Granier et al., 2011), which have no diurnal variation of NO<sub>x</sub> emissions.  
21 The outputs from TM5 model have a horizontal resolution of 1° × 1° and 34 vertical  
22 layers.

23 For the other four numerical experiments (CTRL, CONST, FINE, and MIXED),  
24 WRF-Chem version 4.4 was used to generate *a priori* data (Grell et al., 2005,  
25 Skamarock et al., 2021). The chemistry scheme follows the Regional Atmospheric  
26 Chemistry Mechanism (RACM) with Secondary Organic Aerosol-Volatility Basis Set



1 (SOA-VBS) option (chem\_opt = 108) (Ahmadov et al., 2012). The horizontal  
2 resolution of WRF-Chem simulation is 28 km × 28 km, except for the FINE run (12 km  
3 × 12 km). All simulations have 59 customized vertical layers. To account for the  
4 stratospheric vertical profiles, the Whole Atmosphere Community Climate Model  
5 (WACCM) model outputs were combined with the WRF-Chem data  
6 (ACOM/NCAR/UCAR, 2020, last access: 05 Dec 2022). The combined data comprises  
7 a total of 113 vertical layers. Detailed model configuration is described in Kim et al.  
8 (2024). For the anthropogenic emission inventories, the Air Quality in Northeast Asia  
9 (AQNEA) emission inventory version 2 was adopted. Since the reference year of  
10 AQNEA version 2 is 2019, the anthropogenic NO<sub>x</sub> emissions decreased by 20% to  
11 account for the decreasing trends of NO<sub>x</sub> emissions from 2019 to 2021. We applied the  
12 normalized diurnal variabilities of NO<sub>x</sub> emissions obtained from the Los Angeles Basin  
13 in Kim et al. (2016), but shifting the values one hour earlier (**Figure 1**). For the CONST  
14 run, only the *a priori* profiles at 13:45 LT were used to retrieve the NO<sub>2</sub> TropVCD. To  
15 investigate the impact on the volatile organic compounds (VOC) emissions of the  
16 anthropogenic VOC emissions we used the KORUS emission inventory version 5 (Jang  
17 et al., 2020, Woo et al., 2012) in the MIXED run. We retrieved four months (January,  
18 April, July, and October 2021) for the TM5 and CTRL runs, and one month (July 2021)  
19 for the other runs. The experimental designs are summarized in **Table 1**.

20

### 21 **3. Impacts of different *a priori* data on the retrieved NO<sub>2</sub> TropVCDs**

22 We compared retrieved NO<sub>2</sub> TropVCDs from the five different simulations, or runs, to  
23 study the impacts of *a priori* data used in AMF calculations on the retrieved NO<sub>2</sub>  
24 TropVCD.

#### 25 **3.1. Comparison between the CTRL and TM5 runs**

26 Retrieved NO<sub>2</sub> TropVCDs from the CTRL and TM5 runs exhibit similar diurnal

1 patterns, which are independent of the diurnal patterns of their respective *a priori* data  
2 (**Figure 2**). This suggests that the observed slant column density (SCD) plays a more  
3 decisive role in the diurnal pattern of TropVCD than the influence of *a priori* used to  
4 determine the AMF. Nevertheless, differences in NO<sub>2</sub> TropVCDs between the two runs  
5 were observed, and are particularly noticeable differences in July.

6 **Figure 3** displays spatial distributions of AMF differences between the CTRL  
7 and TM5 runs in January, April, July, and October 2021. In urban areas, the AMF in the  
8 CTRL run was generally lower (blue) than in the TM5 run, but higher values (red) were  
9 observed in the northern and eastern regions of Seoul. As a result, the average values  
10 across the SMA domain were similar between CTRL and TM5 – the diurnal patterns of  
11 averaged air mass factor over the SMA are shown in **Figure 4**. In July, however, lower  
12 values in the CTRL run were observed throughout Seoul and its surrounding areas,  
13 leading to lower average AMF values for the SMA region during most of the day. As a  
14 result, the TropVCD values in July were higher in the CTRL run (Figure 2c).

15 In **Figure 5**, we compare NO<sub>2</sub> vertical profiles at 08, 10, 12, 14, and 16 LT from  
16 the CTRL and TM5 runs. NO<sub>2</sub> values in the lower atmosphere in the CTRL run are  
17 much higher than those in the TM5 run in July, which lead to lower AMF and thus  
18 higher NO<sub>2</sub> TropVCD.

19

### 20 **3.2. Comparisons between the CTRL and CONST, FINE, and MIXED runs**

21 In **Figure 6**, the diurnal patterns of retrieved and *a priori* NO<sub>2</sub> TropVCDs in July 2021  
22 over the SMA region from the CTRL run and the CONST, FINE, and MIXED runs, are  
23 shown. Despite some changes in model resolution and VOC emissions, the FINE and  
24 MIXED runs did not show significant differences compared to the CTRL run. In  
25 particular, the MIXED run resulted in almost no difference in the *a priori* TropVCD ,  
26 resulting in nearly identical retrieved NO<sub>2</sub> TropVCD.

1           On the other hand, the CONST run, which used only the *a priori* vertical profile  
2 from 13:45 LT in the retrieval process, exhibited clear differences to the CTRL run.  
3 Specifically it had lower values than the CTRL run before ~14:00 LT, but higher values  
4 after. These differences are explained by comparisons of vertical profiles from each run,  
5 which are displayed in **Figure 7**. The vertical profile shapes of the CTRL, FINE, and  
6 MIXED runs are identical, indicating that AMF of each runs have similar values. On  
7 the other hand, clear differences of vertical profile shape are apparent between the  
8 CTRL and CONST runs. Before 14:00 LT, the CTRL run showed lower sensitivity in  
9 the upper layers compared to the CONST run. This indicates a smaller AMF and thus  
10 higher VCD values. In contrast, after 14:00 LT, the CTRL run exhibited higher  
11 sensitivity to NO<sub>2</sub> in the upper layers of the troposphere, leading to a larger AMF and  
12 consequently lower VCD values compared to the CONST run. These differences in the  
13 vertical profile arise from effects such as the development of the mixing layer and  
14 variations in emissions throughout the day. This implies that providing optimal time-  
15 dependent *a priori* data for the AMF calculation will improve the accuracy of the  
16 retrieved NO<sub>2</sub> TropVCD.

17

#### 18 **4. Spatiotemporal characteristics of GEMS NO<sub>2</sub> TropVCD**

19 We report on our investigation of the spatiotemporal characteristics of GEMS NO<sub>2</sub>  
20 TropVCD. We use the retrieved NO<sub>2</sub> TropVCD and those simulated by the TM5 and  
21 CTRL runs to assess two geophysically important influences on the NO<sub>2</sub> TropVCD the  
22 SMA region (126.5 – 127.3°E, 37.2 – 37.8°N) in 2021: (1) the identification,  
23 quantification and origin of the seasonal changes; and (2) advection and convection of  
24 air masses.

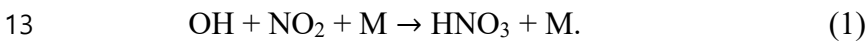
##### 25 **4.1. Seasonal variations**

26 **Figure 2** displays diurnal patterns of retrieved and *a priori* NO<sub>2</sub> TropVCDs during

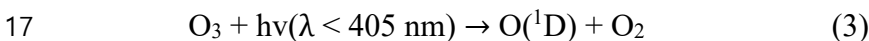
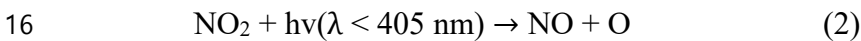
1 weekdays in January, April, July, and October 2021 over the SMA region from the TM5  
2 and CTRL runs. The scenes with wind speed faster than 3m/s are excluded to remove  
3 the transport impacts. The effects of transport on NO<sub>2</sub> columns are analyzed in **Section**  
4 **4.2.**

5 In January, NO<sub>2</sub> TropVCDs continuously increase from 10:00 local time (LT)  
6 to 15:00 LT. During the winter, NO<sub>2</sub> in the urban region accumulates particularly in the  
7 boundary layer. Qualitatively, this is explained as follows.

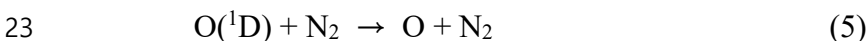
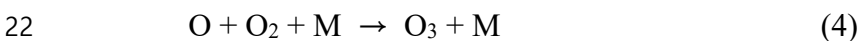
8 As tropospheric solar UV radiation is low in winter and the atmosphere is cold,  
9 photolysis frequencies are small. Similarly, the rate coefficients of many reactions are  
10 smaller at the lower winter temperatures compared to those of the other seasons. In  
11 winter, the relatively slow loss of NO<sub>x</sub> occurs through the three body reaction of  
12 hydroxyl (OH) with NO<sub>2</sub> to form nitric acid (HNO<sub>3</sub>):

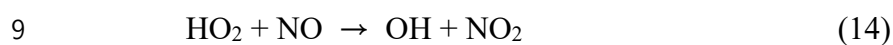
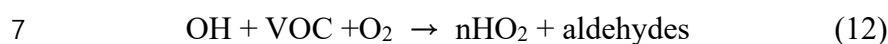
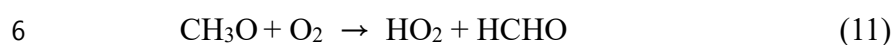
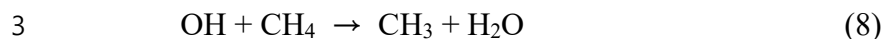
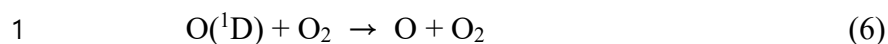


14 The smaller photolysis frequencies of reactions following photoexcitation in the  
15 reactions:



18 lead to slower production of i) the first excited state of oxygen (O(<sup>1</sup>D)) from the  
19 photolysis of ozone (O<sub>3</sub>), ii) the hydroxyl radical (OH), and iii) the production of  
20 organic peroxy radicals (RO<sub>2</sub>), and hydroperoxy (HO<sub>2</sub>) through the oxidation of  
21 methane (CH<sub>4</sub>) and VOC. Some of the following reactions are involved:





10

11 Overall at low solar insolation, the low levels of actinic radiation result in  
12 smaller amounts of OH and HO<sub>2</sub>. The oxidation process is slow and HO<sub>2</sub> and OH  
13 chemistry are coupled with NO<sub>x</sub> chemistry and controlled by rate of oxidation of VOC  
14 and CH<sub>4</sub> and the rate of HO<sub>2</sub> to OH through the rate of reaction (14) and the rate of loss  
15 of HO<sub>x</sub> and NO<sub>x</sub> for example through reaction (1).

16 In January the maximum values of retrieved TropVCDs are  $27.5 \times 10^{15}$  molec.  
17  $\text{cm}^{-2}$  (TM5) and  $28.9 \times 10^{15}$  molec.  $\text{cm}^{-2}$  (CTRL) at 15:00 LT, whereas the *a priori* NO<sub>2</sub>  
18 TropVCDs have maxima of  $11.2 \times 10^{15}$  molec.  $\text{cm}^{-2}$  (TM5) and  $21.9 \times 10^{15}$  molec.  $\text{cm}^{-2}$   
19 (CTRL) at the same time. These higher values of retrieved NO<sub>2</sub> TropVCDs relative to  
20 the model NO<sub>2</sub> TropVCDs are explained by the following inadequate knowledge of the  
21 bottom-up diurnal NO<sub>x</sub> emissions in January and/or the dilution during the transport of

1 plumes, which is dependent on the model horizontal resolution.

2 For other months, the maxima of NO<sub>2</sub> TropVCDs occur at earlier times of the  
3 day in April at 12:00 LT, in July at 10:00 LT and in October at 11:00 LT. There is also  
4 a second maximum at 15:00 LT in October. The behavior of NO<sub>2</sub> TropVCD in April,  
5 July and October, when compared to that in January, is explained by the following  
6 effects: i) faster tropospheric photolysis frequencies, as a result of higher levels of  
7 tropospheric solar insolation and actinic radiation accelerating the photochemical  
8 oxidation of CH<sub>4</sub> and VOC in April, July and October compared to January; ii)  
9 generally faster reaction rate coefficients of the free radical reactions at the higher  
10 temperatures, the rate coefficient of reaction (4) being an exception; iii) the different  
11 diurnal emissions of NO<sub>x</sub> compared to those in January. **Figure 8** shows the diurnal  
12 variations of OH concentrations averaged across boundary layer height in each month,  
13 calculated by the CTRL model run. The OH concentration in January is about an order  
14 of magnitude smaller than that in July.

15 In April, NO<sub>2</sub> TropVCDs increased until 12:00 LT. It then maintains similar  
16 levels until 17:00 LT. The maximum NO<sub>2</sub> TropVCD occurred at 12:00 LT for the CTRL  
17 run ( $21.4 \times 10^{15}$  molec. cm<sup>-2</sup>). The maximum NO<sub>2</sub> TropVCD for the TM5 run appeared  
18 at 17:00 LT, being  $21.9 \times 10^{15}$  molec. cm<sup>-2</sup>. However, the retrieved NO<sub>2</sub> TropVCDs  
19 from the TM5 and CTRL runs have almost identical behavior up to 15:00 LT. There is  
20 a difference of  $1.6 \times 10^{15}$  molec. cm<sup>-2</sup> (8.1%) between the two runs at 17:00 LT, when  
21 *a priori* NO<sub>2</sub> TropVCD value sharply increased from the CTRL run.

22 In July, both the TM5 ( $12.2 \times 10^{15}$  molec. cm<sup>-2</sup>) and CTRL ( $13.9 \times 10^{15}$  molec.  
23 cm<sup>-2</sup>) runs show maxima at 10:00 LT, i.e. the earliest for the four months investigated.  
24 After the peak, NO<sub>2</sub> TropVCDs decrease, most likely due to more rapid photochemical  
25 loss processes e.g. reaction (1) until 14:00 LT, and then increase. In other seasons, the  
26 minimum values were observed in the morning. However, in July, the minimum  
27 occurred at 14:00 LT. This unique pattern of behavior is explained by the more rapid

1 photochemical production and removal reactions in summer. We infer that the chemical  
2 removal becomes relatively more rapid than the emission and production of NO<sub>2</sub> (see  
3 Figure 8). The two types of run show similar diurnal behavior, but the retrieved NO<sub>2</sub>  
4 TropVCD of the CTRL runs between 10:00 and 14:00 LT rise to  $2.1 \times 10^{15}$  molec. cm<sup>-2</sup>  
5 i.e. higher than those of the TM5 runs. The diurnal change of *a priori* NO<sub>2</sub> TropVCDs  
6 from the CTRL runs shows a similar behavior to that of the retrieved NO<sub>2</sub> TropVCDs,  
7 despite the magnitude of *a priori* NO<sub>2</sub> TropVCD being  $3.9 - 8.2 \times 10^{15}$  molec. cm<sup>-2</sup>  
8 higher than those retrieved. On the other hand, the *a priori* NO<sub>2</sub> TropVCD from the  
9 TM5 runs decreases between 08:00 and 14:00 LT, reflecting diurnally varying  
10 photochemistry with similar levels of NO<sub>x</sub> emissions throughout the day.

11 In October, there are broad maxima of NO<sub>2</sub> TropVCD between 12:00 LT and  
12 15:00 LT. Overall diurnal behavior comprises increase up to 12:00 LT, followed by  
13 broad maxima, after which the NO<sub>2</sub> TropVCD are similar to those in April.

14 The highest retrieved values are in the range  $25.1 \times 10^{15}$  to  $25.5 \times 10^{15}$  molec.  
15 cm<sup>-2</sup> for both the TM5 and CTRL runs. As expected, the NO<sub>2</sub> TropVCD are the highest  
16 in January and lowest in July.

17 **Figures 9 and 10** show the spatial distributions of retrieved NO<sub>2</sub> TropVCDs in  
18 January, April, July, and October 2021 from the TM5 and CTRL runs, respectively. In  
19 January, a plume over the SMA region developed as a function of time. Consequently,  
20 the suburban areas, which surround the SMA region, experience relatively high NO<sub>2</sub>  
21 TropVCD ( $> 10 \times 10^{15}$  molec. cm<sup>-2</sup>) compared to that retrieved in the other months. In  
22 April and October, the plumes over the SMA are saturated prior to 12:00 LT and then  
23 decrease. In contrast, the NO<sub>2</sub> TropVCD of the surrounding regions are relatively  
24 constant or even increase. In July, the overall low values cover the SMA and nearby  
25 regions for whole days. The maximum values appear at 10 LT, and then decreased until  
26 14 LT. However, the NO<sub>2</sub> VCD rebounded at 16 LT. **Figure 11** displays the differences  
27 between the TM5 and CTRL runs – red color indicates the CTRL run has higher values

1 than the TM5 run; blue means opposite. The CTRL run shows higher VCD values than  
2 the TM5 run for all times in July. The largest differences over the SMA region are found  
3 at 12 LT in July with differences of  $2.1 \times 10^{15}$  molec.  $\text{cm}^{-2}$ . In other months, the CTRL  
4 run generally have higher values of VCD than the TM5 run over the Seoul and urban  
5 regions, while there are lower values of VCD from the CTRL run over rural regions.

6

## 7 **4.2. Impacts of horizontal transport**

8 **Figure 12** shows the diurnal behavior of the retrieved  $\text{NO}_2$  TropVCDs from the CTRL  
9 run for different wind conditions. The black lines indicate calm runs (wind speed lower  
10 than 3m/s), the green line is a strong-wind run (wind speed faster than 5m/s), and the  
11 blue lines are the average values with no wind filters. In January (Figure 12a), the  
12 diurnal behavior of the  $\text{NO}_2$  TropVCDs change significantly with the wind conditions.  
13 In the calm run (black solid),  $\text{NO}_2$  TropVCD steadily increases due to a combination of  
14 the emissions increasing and the slow chemical loss in this month. In windy runs,  
15 however, diurnal changes in the retrieved  $\text{NO}_2$  TropVCD are negligible.

16 Although the chemical loss is slow during wintertime, the accumulation of  $\text{NO}_2$   
17 was mitigated as strong winds transported large concentrations of  $\text{NO}_2$  to downwind  
18 regions. The differences between calm and other runs were most significant at 15:00  
19 LT, further indicating that continuous outflow due to transport suppressed the  
20 accumulation. As the wind speed increased, there was a noticeable reduction in  $\text{NO}_2$   
21 TropVCD values, which indicates a clear inverse relationship between wind speed and  
22 VCDs, as shown in Edwards et al. (2024). The values of calm, average (blue solid), and  
23 strong wind (green solid) are  $19.0 - 28.9$ ,  $17.2 - 19.8$ , and  $12.1 - 13.4 \times 10^{15}$  molec.  
24  $\text{cm}^{-2}$ , respectively.

25 In April (Figure 12b) and October (Figure 12d), the averaged values with no  
26 wind filters (blue solid) have different diurnal behavior, but the maximum  $\text{NO}_2$



1 TropVCD appear almost simultaneously with that of the calm low wind speed run. In  
2 July (Figure 7c), however, the diurnal behavior from the calm run and no wind filters  
3 are nearly identical, implying that the wind speeds are overall slow in July.

4 In summary, the transport effect is maximized in wintertime, changing not only  
5 the absolute values but also diurnal behavior of NO<sub>2</sub> Trop VCDs. Consequently,  
6 transport must be taken into account when analyzing NO<sub>2</sub> TropVCDs and when  
7 estimating top-down NO<sub>x</sub> emissions. The role of transport needs to be taken into  
8 account even for cases, where the wind speed is relatively slow during summertime  
9 (Yang et al., 2024).

10

## 11 **5. Conclusions**

12 In this study, we analyzed the seasonal variations and diurnal behavior of the retrieved  
13 GEMS IUP-UB NO<sub>2</sub> TropVCD, using the monthly mean data in January, April, July  
14 and October. The effects of wind speed, and the impact of *a priori* NO<sub>2</sub> profiles on the  
15 retrieval. Both in the CTRL and TM5 runs, the GEMS NO<sub>2</sub> product showed significant  
16 changes in quantity, diurnal pattern, and peak time as the seasons changed. In winter,  
17 the values were the highest, with a gradual increase over time, whereas in summer, the  
18 values were the lowest, reaching a minimum in the afternoon. This is consistent with  
19 previous studies, which have shown that atmospheric chemical reactions are more  
20 active in summer. Furthermore, we confirmed that wind-driven transport significantly  
21 influences the diurnal patterns, clearly demonstrating that advection and possibly  
22 convection need to be taken into account when top-down NO<sub>x</sub> emissions are estimated  
23 from an urban agglomeration such as SMA.

24 On the other hand, when using different *a priori* data to calculate VCD values,  
25 more complex results emerged. A comparison between the CTRL and TM5 runs  
26 revealed that, despite different spatial resolution and emission characteristics, the

1 retrieved NO<sub>2</sub> TropVCDs exhibited similar diurnal patterns, with significant differences  
2 only in July. Additionally, we found that the retrieved NO<sub>2</sub> TropVCDs had diurnal  
3 behaviors independent of the *a priori* data in both runs. We infer that the observed SCD  
4 has a stronger influence on the retrieved diurnal patterns than *a priori* profiles.  
5 Adjusting the horizontal resolution of the model (FINE run) or changing the VOC  
6 emissions data (MIXED run) also resulted in no significant differences. However, in  
7 the CONST run, where only the vertical profile at 14:00 LT was used in the retrieval  
8 process throughout the day, there were significant differences in both the NO<sub>2</sub> Trop  
9 VCD values and diurnal patterns. This reaffirms that the vertical shape factor of *a priori*  
10 data plays a critical role in NO<sub>2</sub> TropVCD retrievals.

11         Additionally, given that vertical as well as horizontal model resolution can  
12 influence retrievals (Liu et al., 2020), future studies should analyze the results when the  
13 vertical resolution is adjusted. Furthermore, as highlighted by previous studies, such as  
14 Lorente et al. (2017) and Hong et al. (2017), which emphasized the importance of cloud  
15 parameters, aerosol characteristics, and surface albedo, uncertainties arising from  
16 factors in addition to the *a priori* NO<sub>2</sub> profile should further be investigated in the  
17 retrieval of NO<sub>2</sub> TropVCD for both diurnal GEO observation and those from LEO.

18

## 19 **Data availability**

20 GEMS measurement data retrieved by the IUP algorithm are available on request from  
21 Andreas Richter ([richter@iup.physik.uni-bremen.de](mailto:richter@iup.physik.uni-bremen.de)). WRF-Chem v4.4 is available in  
22 GitHub (wrf-model, 2022).

23

## 24 **Author contributions**

25 SWK initiated this study and secured funding. SS and SWK analyzed the satellite and  
26 model data. SS, KMK, and SWK conducted the model simulations. AR, KL, and JPB

1 provided GEMS IUP products and analyzed the data. JK, JP, HH, HL, UJ retrieved and  
2 analyzed the GEMS observations and discussed the results. JHW provided AQNEA  
3 version 2 emission inventory. SS and SWK wrote the paper, with contributions from all  
4 co-authors.

5

## 6 **Competing interests**

7 At least one of the authors is a member of the editorial board of Atmospheric  
8 Measurement Techniques.

9

## 10 **Acknowledgement**

11 This work was supported by the National Research Foundation of Korea (NRF) grant  
12 funded by the Korea government (MSIT) (No. 2020R1A2C2014131). All the  
13 computing resources are provided by National Center for Meteorological  
14 Supercomputer. Th contributions from the University of Bremen were supported by the  
15 State and University of Bremen and the DLR.

16

## 17 **References**

18 Ahmadov, R., McKeen, S. A., Robinson, A. L., Bahreini, R., Middlebrook, A. M., de  
19 Gouw, J. A., Meagher, J., Hsie, E.-Y., Edgerton, E., Shaw, S., and Trainer, M.: A  
20 volatility basis set model for summertime secondary organic aerosols over the eastern  
21 United States in 2006, *J. Geophys. Res. Atmos.*, 117, D06301,  
22 <https://doi.org/10.1029/2011JD016831>, 2012.

23 Atmospheric Chemistry Observations & Modeling/National Center for Atmospheric  
24 Research/University Corporation for Atmospheric Research: Whole Atmosphere  
25 Community Climate Model (WACCM) Model Output, Research Data Archive at the

1 National Center for Atmospheric Research, Computational and Information System  
2 Laboratory, <https://doi.org/10.5065/G643-Z138>, (last access: 05 December 2022),  
3 2020.

4 Beirle, S., Hörmann, C., Jöckel, P., Liu, S., Penning De Vries, M., Pozzer, A., Sihler, H.,  
5 Valks, P. and Wagner, T.: The STRatospheric Estimation Algorithm from Mainz  
6 (STREAM): Estimating stratospheric NO<sub>2</sub> from nadir-viewing satellites by weighted  
7 convolution, *Atmos. Meas. Tech.*, 9(7), 2753–2779, doi:10.5194/amt-9-2753-2016,  
8 2016.

9 Bovensmann, H., Burrows, J. P., Buchwitz, M., Frerick, J., Noël, S., Rozanov, V. V.,  
10 Chance, K. V., and Gode, A. P. H.: SCIAMACHY: Mission Objectives and  
11 Measurement Modes, *J. Atmos. Sci.*, 56, 127-150, [https://doi.org/10.1175/1520-  
12 0469\(1999\)056<0127:SMOAMM>2.0.CO;2](https://doi.org/10.1175/1520-0469(1999)056<0127:SMOAMM>2.0.CO;2), 1999.

13 Burrows J. P., Hölzle E., Goede A. P. H., Visser H. and Fricke, W.: SCIAMACHY -  
14 Scanning Imaging Absorption Spectrometer for Atmospheric Chartography, *Acta  
15 Astronautica*, 35, 445-461, [https://doi.org/10.1016/0094-5765\(94\)00278-T](https://doi.org/10.1016/0094-5765(94)00278-T), 1995.

16 Burrows, J. P., Weber, M., Buchwitz, M., Rozanov, V., Ladstätter-Weissenmayer, A.,  
17 Richter, A., DeBeek, R., Hoogen, R., Bramstedt, K., Eichmann, K.-U., Elsinger, M.,  
18 and Perner, D.: The Global Ozone Monitoring Experiment (GOME): Mission  
19 Concept and First Scientific Results, *J. Atmos. Sci.*, 56, 151-175,  
20 [https://doi.org/10.1175/1520-0469\(1999\)056<0151:TGOMEG>2.0.CO;2](https://doi.org/10.1175/1520-0469(1999)056<0151:TGOMEG>2.0.CO;2), 1999.

21 Burrows, J. P., Bovensmann, H., Bergametti, G., Flaud, J. M., Orphal, J., Noël, S.,  
22 Monks, P. S., Corlett, G. K., Goede, A. P. H., von Clarmann, T., Steck, T., Fischer,  
23 H., and Friedl-Vallon, F.: The geostationary tropospheric pollution explorer  
24 (GeoTROPE) missions: objects, requirements and mission concept, *Advances in  
25 Space Research*, 34, 682-687, <https://doi.org/10.1016/j.asr.2003.08.067>, 2004.

26 Callies, J., Corpaccioli, E., Eisinger, M., Hahne, A., and Lefebvre, A.: GOME-2-

1 Metop's second-generation sensor for operational ozone monitoring, *ESA Bulletin*,  
2 102, 28–36, 2000.

3 Edwards, D. P., Martínez-Alonso, S., Jo, D.-S., Ortega, I., Emmons, L. K., Orlando, J.  
4 J., Worden, H. M., Kim, J., Lee, H., Park, J., and Hong, H.: Quantifying the diurnal  
5 variation of atmospheric NO<sub>2</sub> from observations of the Geostationary Environment  
6 Monitoring Spectrometer (GEMS), *Atmos. Chem. Phys.*, 24, 8943-8961,  
7 <https://doi.org/10.5194/acp-24-8943-2024>, 2024.

8 Granier, C., Bessagnet, B., Bond, T., D'Angiola, A., van der Gon, H. D., Frost, G. J.,  
9 Heil, A., Kaiser, J. W., Kinne, S., Klimont, Z., Kloster, S., Lamarque, J.-F., Liousse,  
10 C., Masui, T., Meleux, F., Mieville, A., Ohara, T., Raut, J.-C., Riahi, K., Schultz, M.  
11 G., Smith, S. J., Thompson, A., van Aardenne, J., van der Warf, G. R., and van Vuuren,  
12 D. P.: Evolution of anthropogenic and biomass burning emissions of air pollutants at  
13 global and regional scales during the 1980 – 2010 period, *Climatic Change*, 109, 163,  
14 <https://doi.org/10.1007/s10584-011-0154-1>, 2011.

15 Grell, G. A., Peckham, S. E., Schmitz, R., McKeen, S. A., Frost, G., Shamarock, W. C.,  
16 and Eder, B.: Fully coupled “online” chemistry within the WRF model, *Atmos.*  
17 *Environ.*, 39, 6957-6975, <https://doi.org/10.1016/j.atmosenv.2005.04.027>, 2005.

18 Hong, H., Lee, H., Kim, J., Jeong, U., Ryu, J., Lee, D. S.: Investigation of Simultaneous  
19 Effects of Aerosol Properties and Aerosol Peak Height on the Air Mass Factors for  
20 Space-Borne NO<sub>2</sub> Retrievals, *remote sens.*, 9(3), 208,  
21 <https://doi.org/10.3390/rs9030208>, 2017.

22 Huijnen, V., Williams, J., van Weele, M., van Noije, T., Krol, M., Dentener, F., Segers,  
23 A., Houweling, S., Peters, W., de Laat, J., Boersma, F., Bergamaschi, P., van  
24 Velthoven, P., Le Sager, P., Eskes, H., Alkemade, F., Scheele, R., Nédélec, P., and  
25 Pätz, H.-W.: The global chemistry transport model TM5: description and evaluation  
26 of the tropospheric chemistry version 3.0, *Geosci. Model Dev.*, 3, 445-473,

1 <https://doi.org/10.5194/gmd-3-445-2010>, 2010.

2 Jang, Y., Lee, Y., Kim, J., Kim, Y., and Woo, J.-H.: Improvement China point source for  
3 improving bottom-up emission inventory, *Asia-Pac. J. Atmos. Sci.*, 56, 107-118,  
4 <https://doi.org/10.1007/s13143-019-00115-y>, 2020.

5 Kim, J., Jeong, U., Ahn, M.-H., Kim, J. H., Park, R. J., Lee, H., Song, C. H., Choi, Y.-  
6 S., Lee, K.-J., Yoo, J.-M., Jeong, M.-J., Park, S. K., Lee, K.-M., Song, C.-K., Kim,  
7 S.-W., Kim, Y. J., Kim, S.-W., Kim, M., Go, S., Liu, X., Chance, K., Miller, C. C.,  
8 Al-Saadi, J., Veihelmann, B., Bhartia, P. K., Torres, O., González Abad, G., Haffner,  
9 D. P., Ko, D. H., Lee, S. H., Woo, J.-H., Chong, H., Park, S. S., Nicks, D., Choi, W.  
10 J., Moon, K.-J., Cho, A., Yoon, J., Kim, S.-K., Hong, H., Lee, K., Lee, H., Lee, S.,  
11 Choi, M., Veekfind, P., Levelt, P. F., Edwards, D. P., Kang, M., Eo, M., Bak, J., Baek,  
12 K., Kwon, H.-A., Yang, J., Park, J., Han, K. M., Kim, B.-R., Shin, H.-W., Choi, H.,  
13 Lee, E., Chong, J., Cha, Y., Koo, J.-H., Irie, H., Hayashida, S., Kasai, Y., Kanaya, Y.,  
14 Liu, C., Lin, J., Crawford, J. H., Carmichael, G. R., Newchurch, M. J., Lefter, B. L.,  
15 Herman, J. R., Swap, R. J., Lau, A. K. H., Kurosu, T. P., Jaross, G., Ahlers, B., Dobber,  
16 M., McElroy, C. T., and Choi, Y.: New Era of Air Quality Monitoring from Space:  
17 Geostationary Environment Monitoring Spectrometer (GEMS), *Bull. Amer. Meteor.*  
18 *Soc.*, 101, E1-E22, <https://doi.org/10.1175/BAMS-D-18-0013.1>, 2020.

19 Kim, K.-M., Kim, S.-W., Seo, S., Blake, D. R., Cho, S., Crawford, J. H., Emmons, L.  
20 K., Fried, A., Herman, J. R., Hong, J., Jung, J., Pfister, G. G., Weinheimer, A. J., Woo,  
21 J.-H., and Zhang, Q.: Sensitivity of the WRF-Chem v4.4 simulations of ozone and  
22 formaldehyde and their precursors to multiple bottom-up emission inventories over  
23 East Asia during the KORUS-AQ 2016 field campaign, *Geosci. Model Dev.*, 17,  
24 1931-1955, <https://doi.org/10.5194/gmd-17-1931-2024>, 2024.

25 Kim, S.-W., McDonald, B. C., Brown, S. S., Dube, B., Ferrare, R. A., Frost, G. J., Harley,  
26 R. A., Holloway, J. S., Lee, H.-J., McKeen, S. A., Neuman, J. A., Nowak, J. B., Oetjen,  
27 H., Ortega, I., Pollack, I. B., Roberts, J. M., Ryerson, T. B., Scarino, A. J., Senff, C.

1 J., Thalman, R., Trainer, M., Volkamer, R., Wagner, N., Washenfelder, R. A., Waxman,  
2 E., and Young, C. J.: Modeling the weekly cycle of NO<sub>x</sub> and CO emissions and their  
3 impacts on O<sub>3</sub> in the Los Angeles-South Coast Air Basin during the CalNex 2010  
4 field campaign, *J. Geophys. Res. Atmos.*, 121, 1340-1360,  
5 <https://doi.org/10.1002/2015JD024292>, 2016.

6 Lange, K., Richter, Bösch, T., Zilker, B., Latsch, M., Behrens, L. K., Okafor, C. M.,  
7 Bösch, H., Burrows, J. P., Merlaud, A., Pinaridi, G., Fayt, C., Friedrich, M. M.,  
8 Dimitropoulou, E., Van Roozendael, M., Ziegler, S., Ripperger-Lukosiunaite, S.,  
9 Kuhn, L., Lauster, B., Wagner, T., Hong, H., Kim, D., Chang, L.-S., Bae, K., Song,  
10 C.-K., and Lee, H.: Validation of GEMS tropospheric NO<sub>2</sub> columns and their diurnal  
11 variation with ground-based DOAS measurements, *EGUsphere [preprint]*,  
12 <https://doi.org/10.5194/egusphere-2024-617>, 2024.

13 Levelt, P. F., van den Oord, G. H. J., Dobber, M., R., Mälkki, A., Visser, H., de Vries,  
14 J., Stammes, P., Lundell, J. O. V., and Saari, H.: The Ozone Monitoring Instrument,  
15 *IEEE Trans. Geosci. Remote Sens.*, 44(5), 1093-1101,  
16 <https://doi.org/10.1109/TGRS.2006.872333>, 2006.

17 Liu, S., Valks, P. Pinaridi, G., Xu, J., Argyrouli, A., Lutz, R., Tilstra, G., Huijnen, V.,  
18 Hendric, F., and Van Roozendael, M.: An improved air mass factor calculation for  
19 nitrogen dioxide measurements from the Global Ozone Monitoring Experiment-2  
20 (GOME-2), *Atmos. Meas. Tech.*, 13, 755-787, [https://doi.org/10.5194/amt-13-755-](https://doi.org/10.5194/amt-13-755-2020)  
21 [2020](https://doi.org/10.5194/amt-13-755-2020), 2020.

22 Lorente, A., Boersma, K. F., Yu, H., Dörner, S., Hilboll, A., Richter, A., Liu, M., Lamsal,  
23 L. N., Barkley, M., De Smedt, I., Van Roozendael, M., Wang, Y., Wagner, T., Beirle,  
24 S., Lin, J.-T., Krotkov, N., Stammes, P., Wang, P., Eskes, H. J., and Krol, M.:  
25 Structural uncertainty in air mass factor calculation for NO<sub>2</sub> and HCHO satellite  
26 retrievals, *Atmos. Mech. Tech.*, 10, 759-782, [https://doi.org/10.5194/amt-10-759-](https://doi.org/10.5194/amt-10-759-2017)  
27 [2017](https://doi.org/10.5194/amt-10-759-2017), 2017.

- 1 Milford, J. B., Russell, A. G., and McRae, G. J.: A new approach to photochemical  
2 pollution control: implications of spatial patterns in pollutant responses in nitrogen  
3 oxides and reactive organic gas emissions, *Environ. Sci. Technol.*, 23, 1290-1301,  
4 <https://doi.org/10.1021/es00068a017>, 1989.
- 5 Munro, R., Lang, R., Klaes, D., Poli, G., Retscher, C., Lindstrot, R., Huckle, R., Lacan,  
6 A., Grzegorski, M., Holdak, A., Kokhanovsky, A., Livschitz, J., and Eisinger, M.:  
7 The GOME-2 instrument on the Metop series of satellites: instrument design,  
8 calibration, and level 1 data processing – an overview, *Atmos. Meas. Tech.*, 9, 1279–  
9 1301, <https://doi.org/10.5194/amt-9-1279-2016>, 2016.
- 10 Palmer, P. I., Jacob, D. J., Chance, K., Martin, R. V., Spurr, R. J. D., Kurosu, T. P., Bey,  
11 I., Yantosca, R., Fiore, A., and Li, Q.: Air mass factor formulation for spectroscopic  
12 measurements from satellites: Application to formaldehyde retrievals from the  
13 Global Ozone Monitoring Experiment, *J. Geophys. Res.*, 106, 14539-14550,  
14 <https://doi.org/10.1029/2000JD900772>., 2001.
- 15 Richter, A. and Burrows, J. P.: Tropospheric NO<sub>2</sub> from GOME Measurements,  
16 *Advances in Space Research*, 29, 1673-1683, [https://doi.org/10.1016/S0273-  
17 1177\(02\)00100-X](https://doi.org/10.1016/S0273-1177(02)00100-X), 2002.
- 18 Richter, A., Lange, K., Burrows, J. Bösch, J., Kim, S.-W., Seo, S., Kim, K.-M., Hong,  
19 H., Lee, H., and Park, J.: An improved tropospheric NO<sub>2</sub> retrieval for GEMS, *Atmos.*  
20 *Meas. Tech.*, in preparation, 2024.
- 21 Rozanov, V. V., Rozanov, A. V., Kokhanovsky, A. A. and Burrows, J. P.: Radiative  
22 transfer through terrestrial atmosphere and ocean: Software package SCIATRAN, *J.*  
23 *Quant. Spectrosc. Radiat. Transf.*, 133, 13–71,  
24 <https://doi.org/10.1016/j.jqsrt.2013.07.004>, 2014.
- 25 Skamarock, W. C., Klemp, J. B., Dudhia, J., Gill, D. O., Liu, Z., Berner, J., Wang, W.,  
26 Powers, J. G., Duda, M. G., Barker, D. M., Huang, X.-Y.: A Description of the



1 Advanced Research WRF Model Version 4 (No. NCAR/TN-556+STR),  
2 <https://doi.org/10.5065/1dfh-6p97>, 2021.

3 Tilstra, L. G., de Graaf, M., Trees, V. J. H., Litvinov, P., Dubovik, O., and Stammes, P.:  
4 A directional surface reflectance climatology determined from TROPOMI  
5 observations, *Atmos. Meas. Tech.*, 17, 2235-2256, [https://doi.org/10.5194/amt-17-](https://doi.org/10.5194/amt-17-2235-2024)  
6 [2235-2024](https://doi.org/10.5194/amt-17-2235-2024), 2024.

7 Veefkind, J. P., Aben, I., McMullan, K. Förster, H., de Vries, J., Otter, G., Claas, J.,  
8 Eskes, H. J., de Haan, J. F., Kleipool, Q., van Weele, M., Hasekamp, O., Hoogeveen,  
9 R., Landgraf, J., Snel, R., Tol, P., Ingmann, P., Voors, R., Kruizinga, B., Vink, R.,  
10 Visser, H., and Levelt, P. F.: TROPOMI on the ESA Sentinel-5 Precursor: A GMES  
11 mission for global observations of the atmospheric composition for climate, air  
12 quality and ozone layer applications, *Remote Sens. Environ.*, 120, 70-83,  
13 <https://doi.org/10.1016/j.rse.2011.09.027>, 2012.

14 Williams, J. E., Boersma, K. F., Le Sager, P., and Verstraeten, W. W.: The high-  
15 resolution version of TM5-MP for optimized satellite retrievals: description and  
16 validation, *Geosci. Model Dev.*, 10, 721–750, [https://doi.org/10.5194/gmd-10-721-](https://doi.org/10.5194/gmd-10-721-2017)  
17 [2017](https://doi.org/10.5194/gmd-10-721-2017), 2017.

18 Woo, J.-H., Choi, K.-C., Kim, H. K., Baek, B. H., Jang, M., Eum, J.-H., Song, C. H.,  
19 Ma, Y.-I., Sunwoo, Y., Chang, L.-S., and Yoo, S. H.: Development of an  
20 anthropogenic emissions processing system for Asia using SMOKE, *Atmos. Environ.*,  
21 58, 5-13, <https://doi.org/10.1016/j.atmosenv.2011.10.042>, 2012.

22 wrf-model: WRF, Github [code], <https://github.com/wrf-model/WRF/release/tag/v4.4>,  
23 last access: 18 May 2022.

24 Yang, L. H., Jacob, D. J., Dang, R., Oak, Y. J., Lin, H., Kim, J., Zhai, S., Colombi, N.  
25 K., Pendergrass, D. C., Beaudry, E., Shah, V., Feng, X., Yantosca, R. M., Chong, H.,  
26 Park, J., Lee, H., Lee, W.-J., Kim, S., Kim, E., Travis, K. R., Crawford, J. H., Liao,

1 H., Interpreting GEMS geostationary satellite observations of the diurnal variation  
2 of nitrogen dioxide (NO<sub>2</sub>) over East Asia, *Atmos. Chem. Phys.*,  
3 <https://doi.org/10.5194/acp-24-7027-2024>, 2024.

1 **List of Tables**

- 2 **Table 1.** Description of the experimental designs. MACCity provides hourly-constant  
3 emissions, while the others provide hourly-varying emissions.

1 **List of Figures**

2 **Figure 1.** Diurnal variabilities of normalized NO<sub>x</sub> emissions for CTRL (black) and  
3 TM5 (gray) runs over the SMA region.

4 **Figure 2.** Diurnal behavior of retrieved (solid) and *a priori* (dashed) NO<sub>2</sub> TropVCDs  
5 during weekdays in (a) January, (b) April, (c) July, and (d) October 2021 over the SMA  
6 region. Gray lines identify the TM5 run, while black lines represent the CTRL run. The  
7 pixels with wind speed faster than 3m/s are excluded.

8 **Figure 3.** Spatial distributions of air mass factor (AMF) differences (CTRL – TM5) in  
9 January, April, July, and October 2021. The pixels with wind speed faster than 3m/s are  
10 excluded.

11 **Figure 4.** Diurnal patterns of the air mass factor during weekdays in (a) January, (b)  
12 April, (c) July, and (d) October 2021 over the SMA region. Gray lines indicate the TM5  
13 run, while black lines mean the CTRL run. The pixels with wind speed faster than 3m/s  
14 are excluded.

15 **Figure 5.** Vertical profiles of *a priori* NO<sub>2</sub> mixing ratios at 08, 10, 12, 14, and 16 LT  
16 from the TM5 (gray) and CTRL (black) runs in January, April, July, and October 2021  
17 over the SMA region.

18 **Figure 6.** Diurnal patterns of retrieved (solid) and *a priori* (dashed) NO<sub>2</sub> TropVCDs in  
19 July 2021 over SMA region from the CTRL run (black) and (a) CONST run (red), (b)  
20 FINE run (pink), and (c) MIXED run (yellow). The pixels with wind speed faster than  
21 3m/s are excluded. Note that diurnal changes of *a priori* NO<sub>2</sub> TropVCDs in the CONST  
22 run occur during calculating domain-averaged values – the location and number of  
23 pixels excluded during the collocation with satellite data vary over time during the day.

24 **Figure 7.** Vertical profiles of *a priori* NO<sub>2</sub> mixing ratios at 08, 10, 12, 14, and 16 LT  
25 from the CTRL (black), CONST (red), FINE (pink), and MIXED run (yellow) in  
26 January, April, July, and October 2021 over the SMA region.

1 **Figure 8.** Diurnal patterns of boundary layer mean OH concentrations over the SMA  
2 region in January (black), April (yellow), July (red), and October (blue) 2021 from the  
3 CTRL run.

4 **Figure 9.** Spatial distributions of retrieved NO<sub>2</sub> TropVCDs in January, April, July, and  
5 October 2021 taking the a priori data for the AMF from the TM5 run. The scenes with  
6 wind speed faster than 3m/s are excluded to minimize the impact of rapid transport.

7 **Figure 10.** Same as Figure 9, except that *a priori* values for the AMF calculation are  
8 taken from the CTRL run.

9 **Figure 11.** Similar to Figure 9, but for the differences of NO<sub>2</sub> TropVCD between CTRL  
10 and TM5 run (CTRL – TM5).

11 **Figure 12.** Diurnal patterns of retrieved NO<sub>2</sub> TropVCDs from the CTRL run in (a)  
12 January, (b) April, (c) July, and (d) October 2021 over the SMA region. Black lines  
13 indicate the NO<sub>2</sub> TropVCD values with wind-filtered data; only the scenes with wind  
14 speed lower than 3m/s are utilized. Blue lines are the averaged values without any wind  
15 filters. The green line is for case of strong-wind run with the NO<sub>2</sub> TropVCD being  
16 selected and averaged for wind speeds faster than 5m/s in January.

17

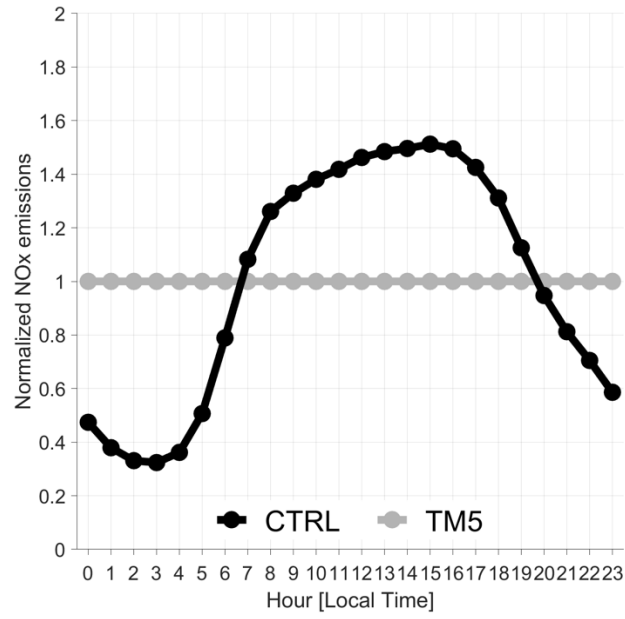
1 **Table 1.** Description of the experimental designs. MACCity provides hourly-constant  
 2 emissions, while the others provide hourly-varying emissions.

<b>Run name</b>	<b>Model</b>	<b>Horizontal resolution</b>	<b>Emission inventory</b>
TM5	TM5	1° × 1°	MACCity
CTRL		28 × 28 km <sup>2</sup>	2021AQNEA
CONST <sup>a)</sup>	WRF-Chem v4.4	28 × 28 km <sup>2</sup>	2021AQNEA
FINE		12 × 12 km <sup>2</sup>	2021AQNEA
MIXED		28 × 28 km <sup>2</sup>	(VOC) KORUSv5 (others) 2021AQNEA

3

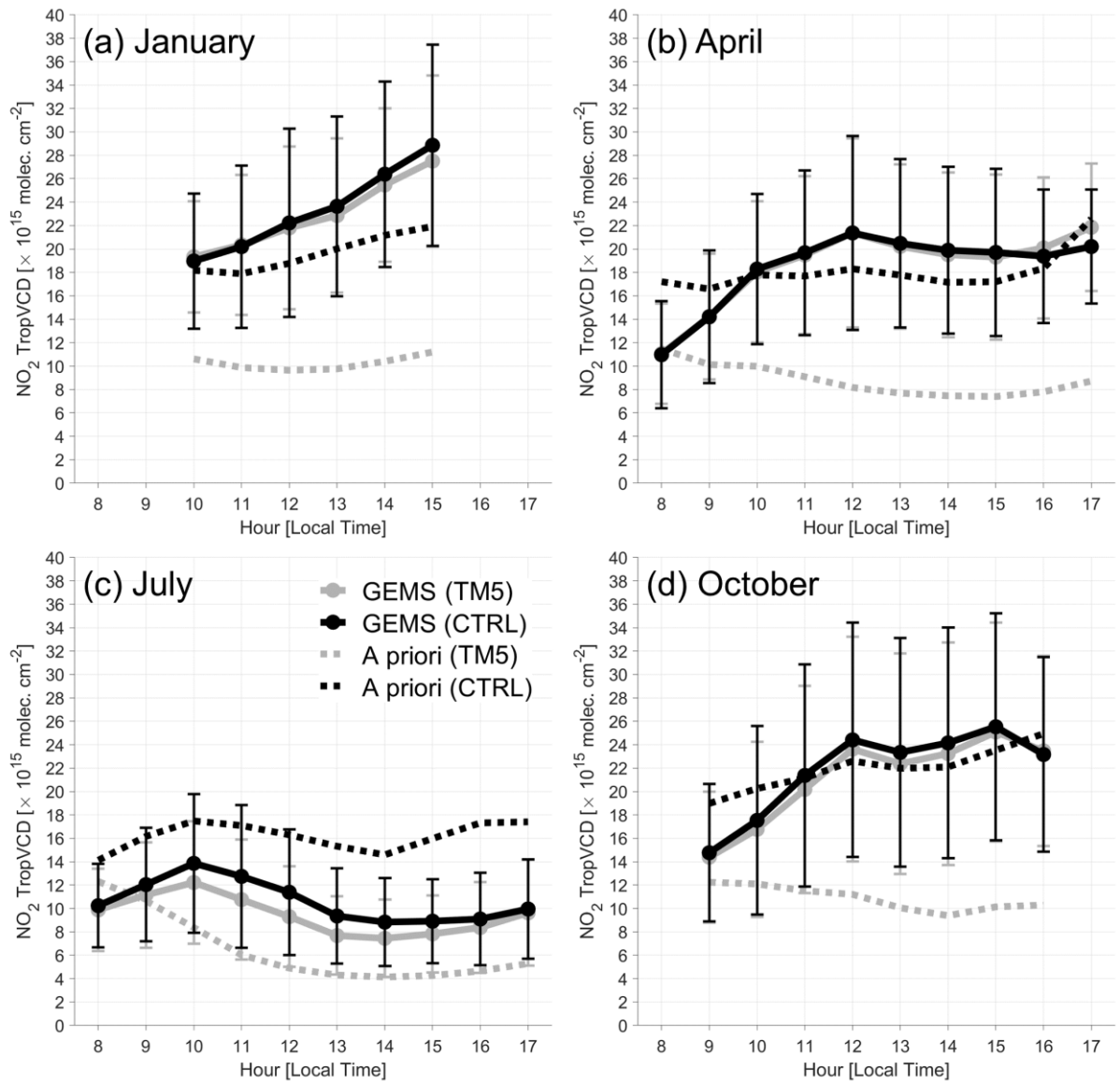
4 <sup>a)</sup> CONST run uses hourly-varying emission inventory, but only data of 13:45 LT were  
 5 utilized to compute AMF.

6



1

2 **Figure 1.** Diurnal variabilities of normalized NOx emissions for CTRL (black) and  
3 TM5 (gray) runs over the SMA region.



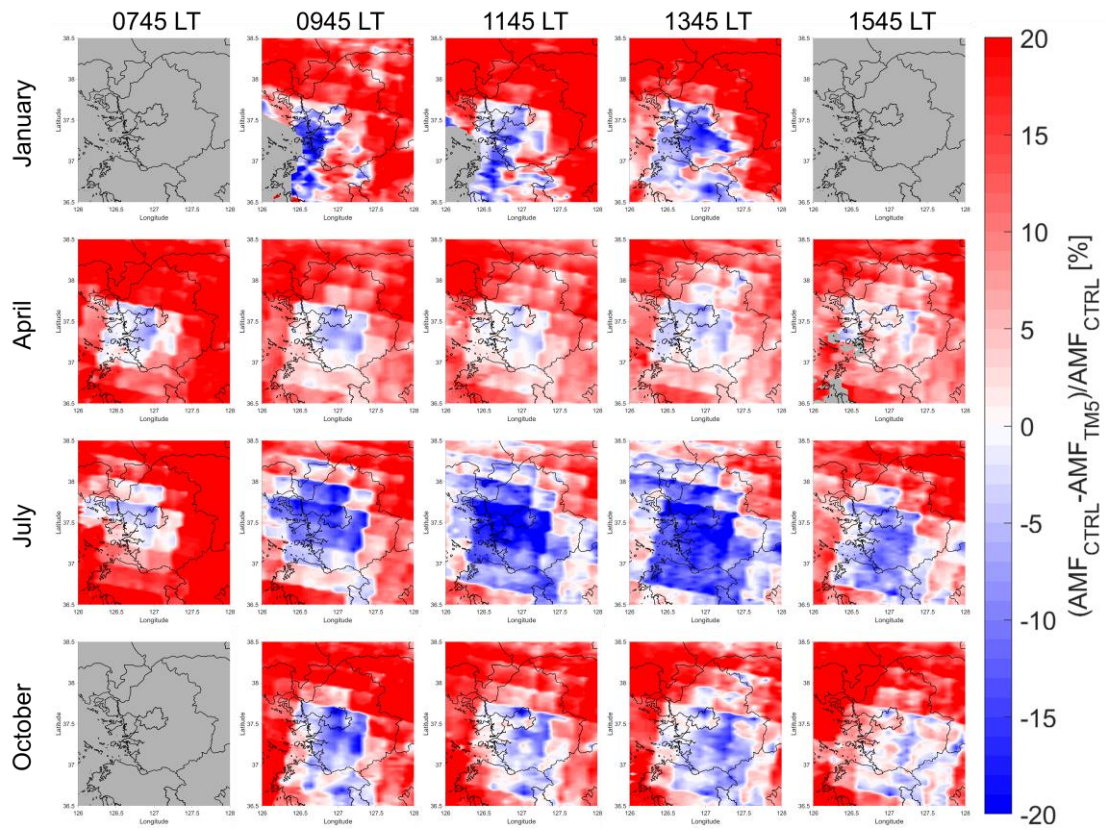
1

2 **Figure 2.** Diurnal behavior of retrieved (solid) and *a priori* (dashed) NO<sub>2</sub> TropVCDs  
 3 during weekdays in (a) January, (b) April, (c) July, and (d) October 2021 over the SMA  
 4 region. Gray lines identify the TM5 run, while black lines represent the CTRL run. The  
 5 pixels with wind speed faster than 3m/s are excluded.

6

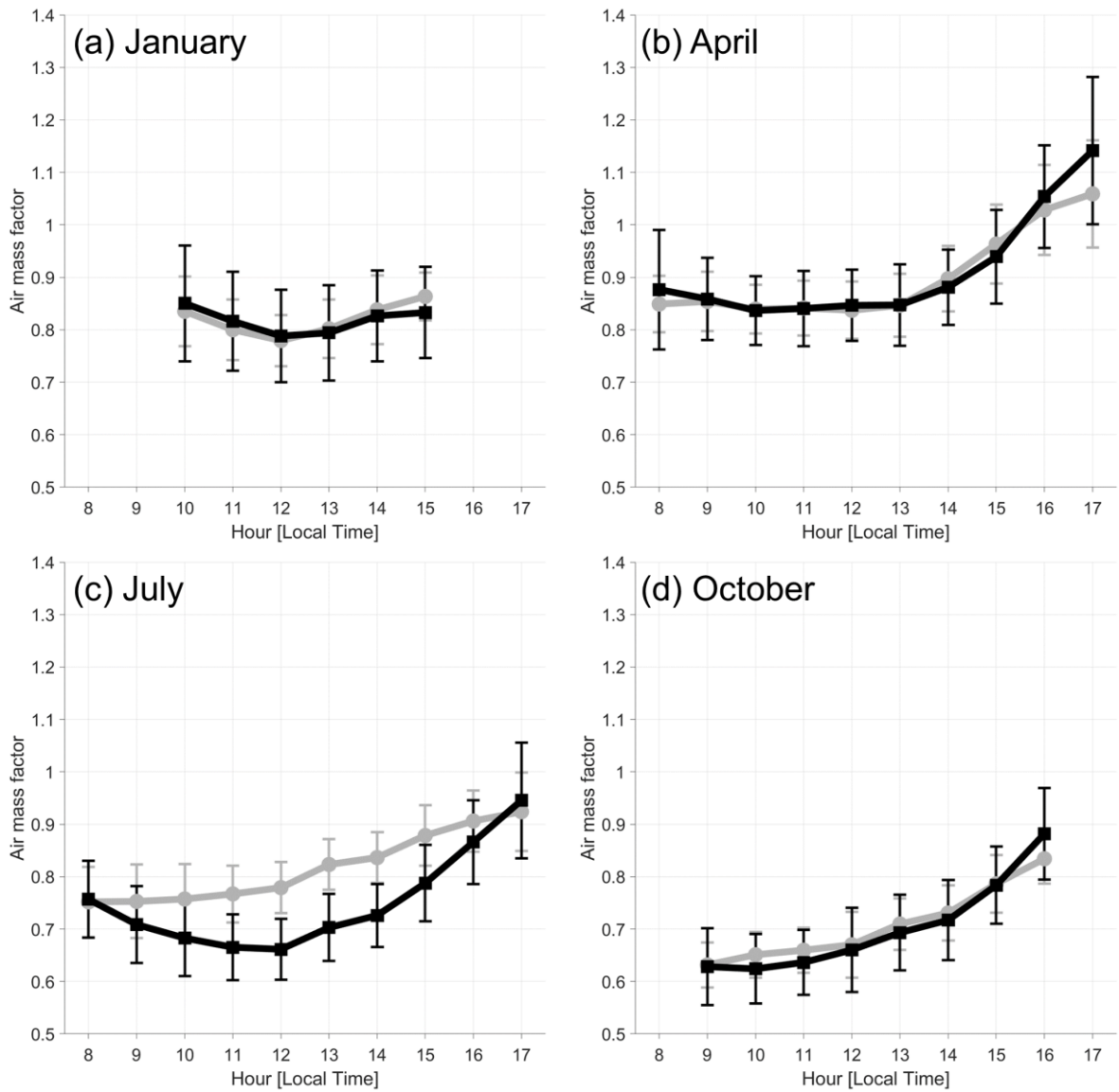
7





1

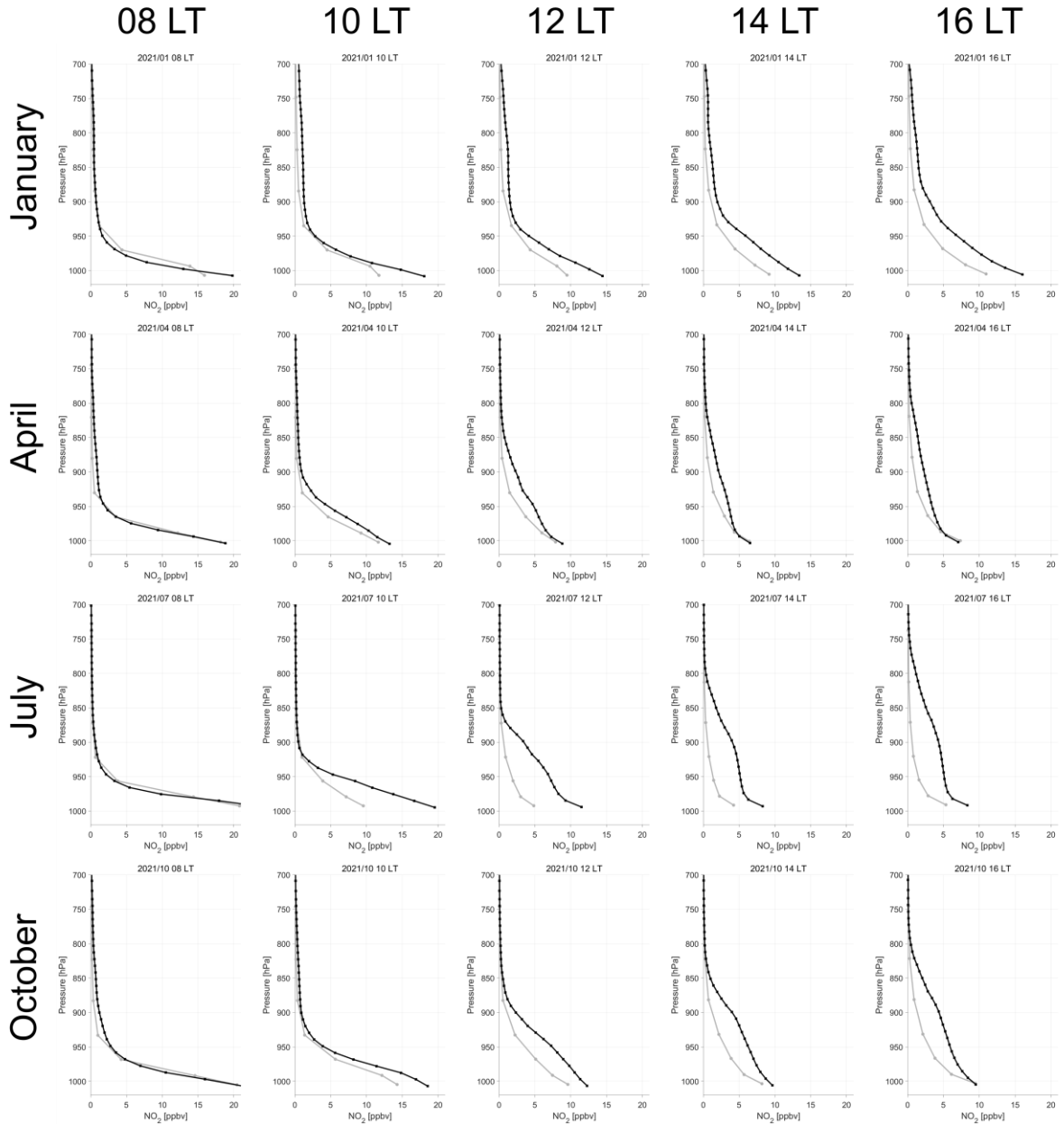
2 **Figure 3.** Spatial distributions of air mass factor (AMF) differences (CTRL – TM5) in  
 3 January, April, July, and October 2021. The pixels with wind speed faster than 3m/s are  
 4 excluded.



1

2 **Figure 4.** Diurnal patterns of the air mass factor during weekdays in (a) January, (b)  
 3 April, (c) July, and (d) October 2021 over the SMA region. Gray lines indicate the TM5  
 4 run, while black lines mean the CTRL run. The pixels with wind speed faster than 3m/s  
 5 are excluded.

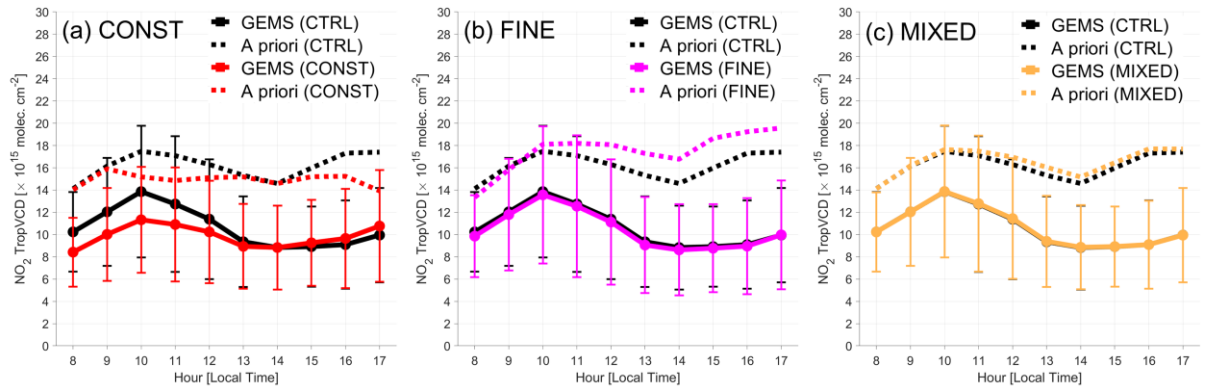
6



1

2 **Figure 5.** Vertical profiles of *a priori* NO<sub>2</sub> mixing ratios at 08, 10, 12, 14, and 16 LT  
 3 from the TM5 (gray) and CTRL (black) runs in January, April, July, and October  
 4 over the SMA region.

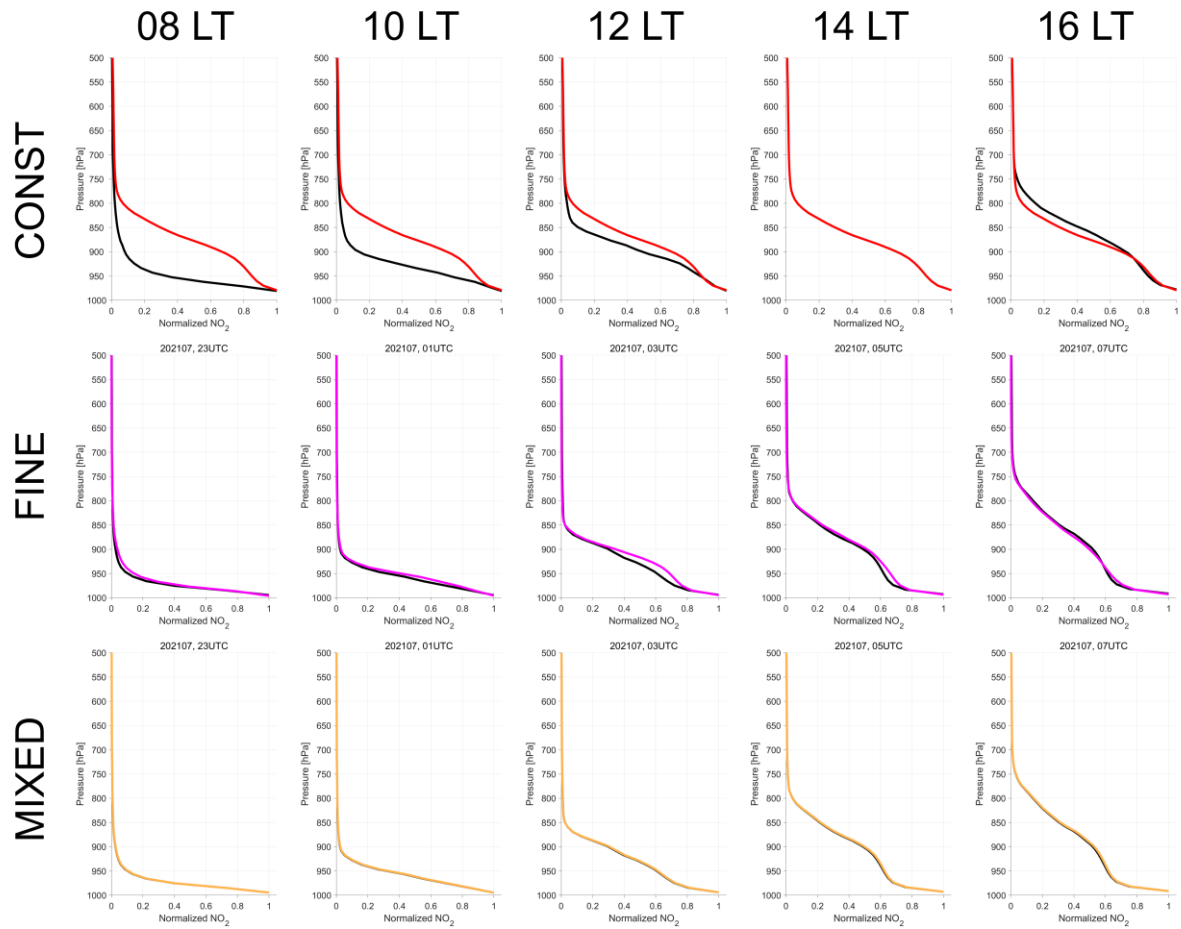
5



1

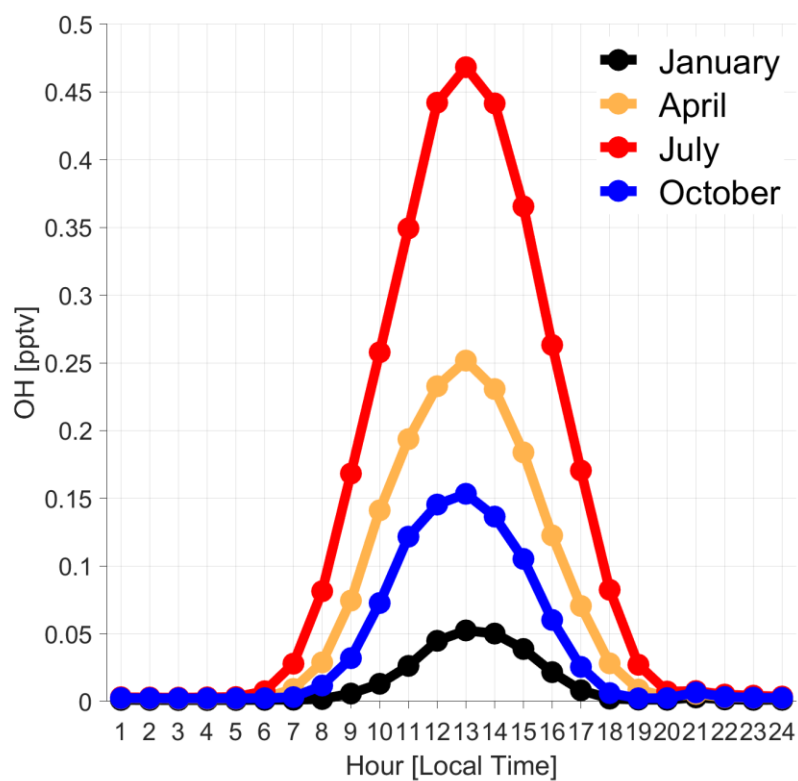
2 **Figure 6.** Diurnal patterns of retrieved (solid) and *a priori* (dashed) NO<sub>2</sub> TropVCDs in  
 3 July 2021 over SMA region from the CTRL run (black) and (a) CONST run (red), (b)  
 4 FINE run (pink), and (c) MIXED run (yellow). The pixels with wind speed faster than  
 5 3m/s are excluded. Note that diurnal changes of *a priori* NO<sub>2</sub> TropVCDs in the CONST  
 6 run occur during calculating domain-averaged values – the location and number of  
 7 pixels excluded during the collocation with satellite data vary over time during the day.

8



1

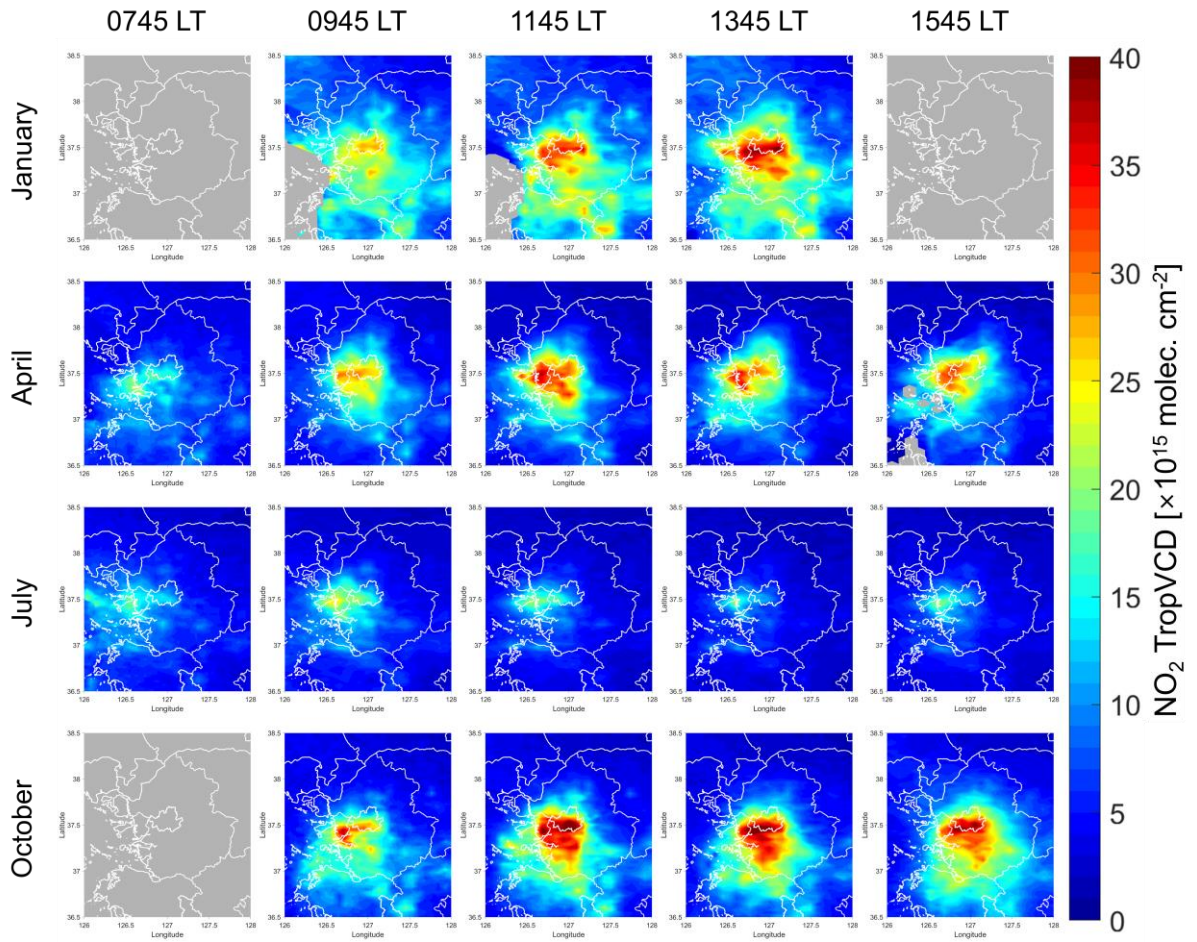
2 **Figure 7.** Vertical profiles of *a priori* NO<sub>2</sub> mixing ratios at 08, 10, 12, 14, and 16 LT  
 3 from the CTRL (black), CONST (red), FINE (pink), and MIXED run (yellow) in  
 4 January, April, July, and October 2021 over the SMA region.



1

2 **Figure 8.** Diurnal patterns of boundary layer mean OH concentrations over the SMA  
 3 region in January (black), April (yellow), July (red), and October (blue) 2021 from the  
 4 CTRL run.

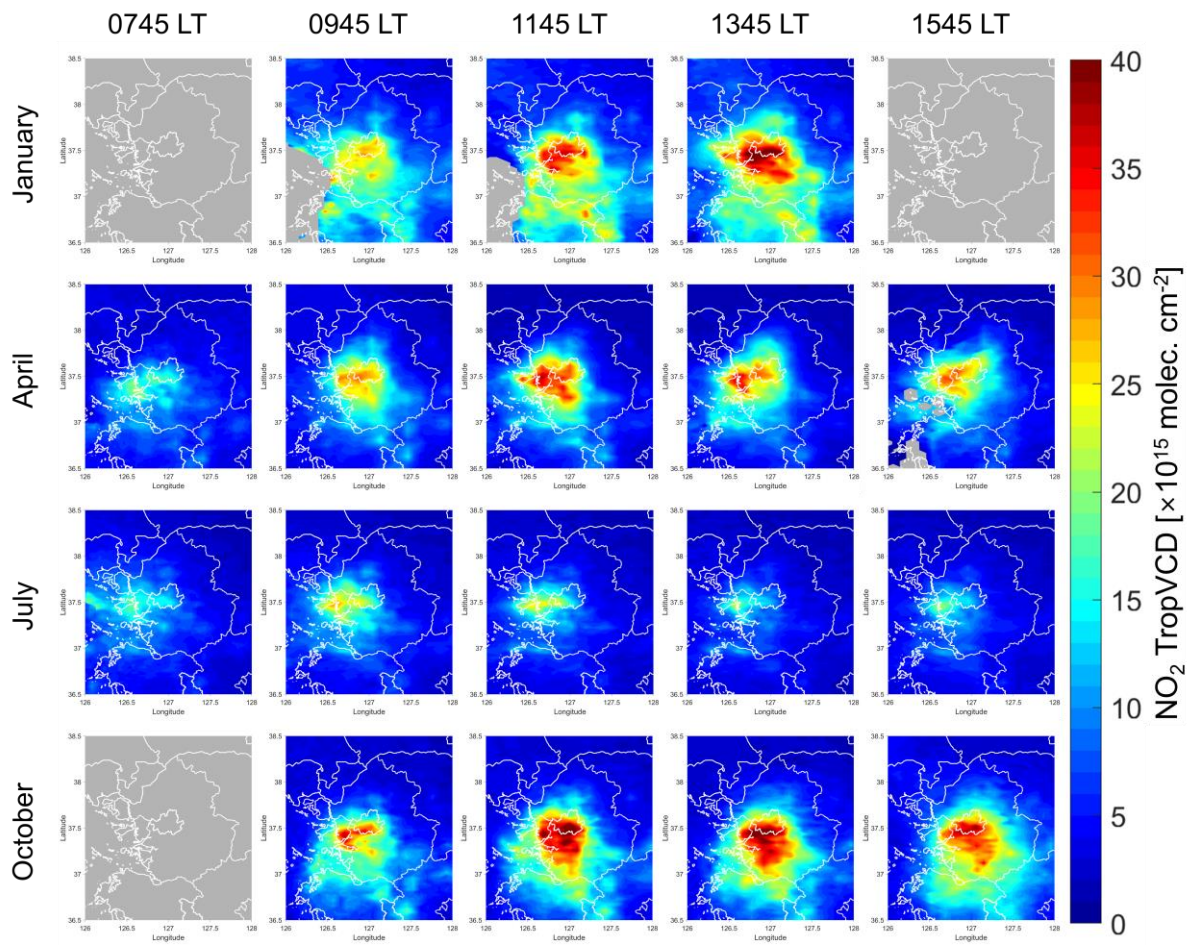
5



1

2 **Figure 9.** Spatial distributions of retrieved NO<sub>2</sub> TropVCDs in January, April, July, and  
 3 October 2021 taking the a priori data for the AMF from the TM5 run. The scenes with  
 4 wind speed faster than 3m/s are excluded to minimize the impact of rapid transport.

5

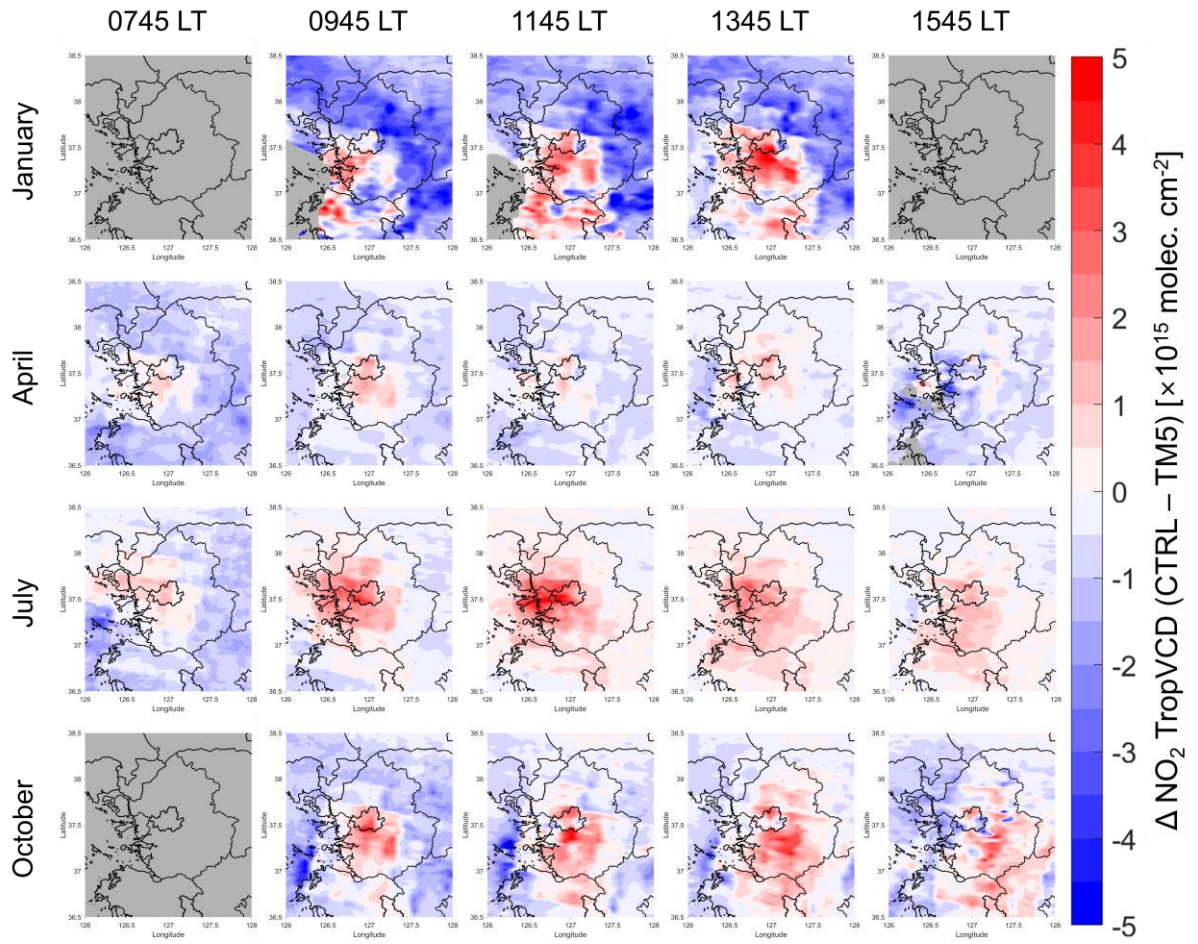


1

2 **Figure 10.** Same as Figure 9, except that *a priori* values for the AMF calculation are  
 3 taken from the CTRL run.

4

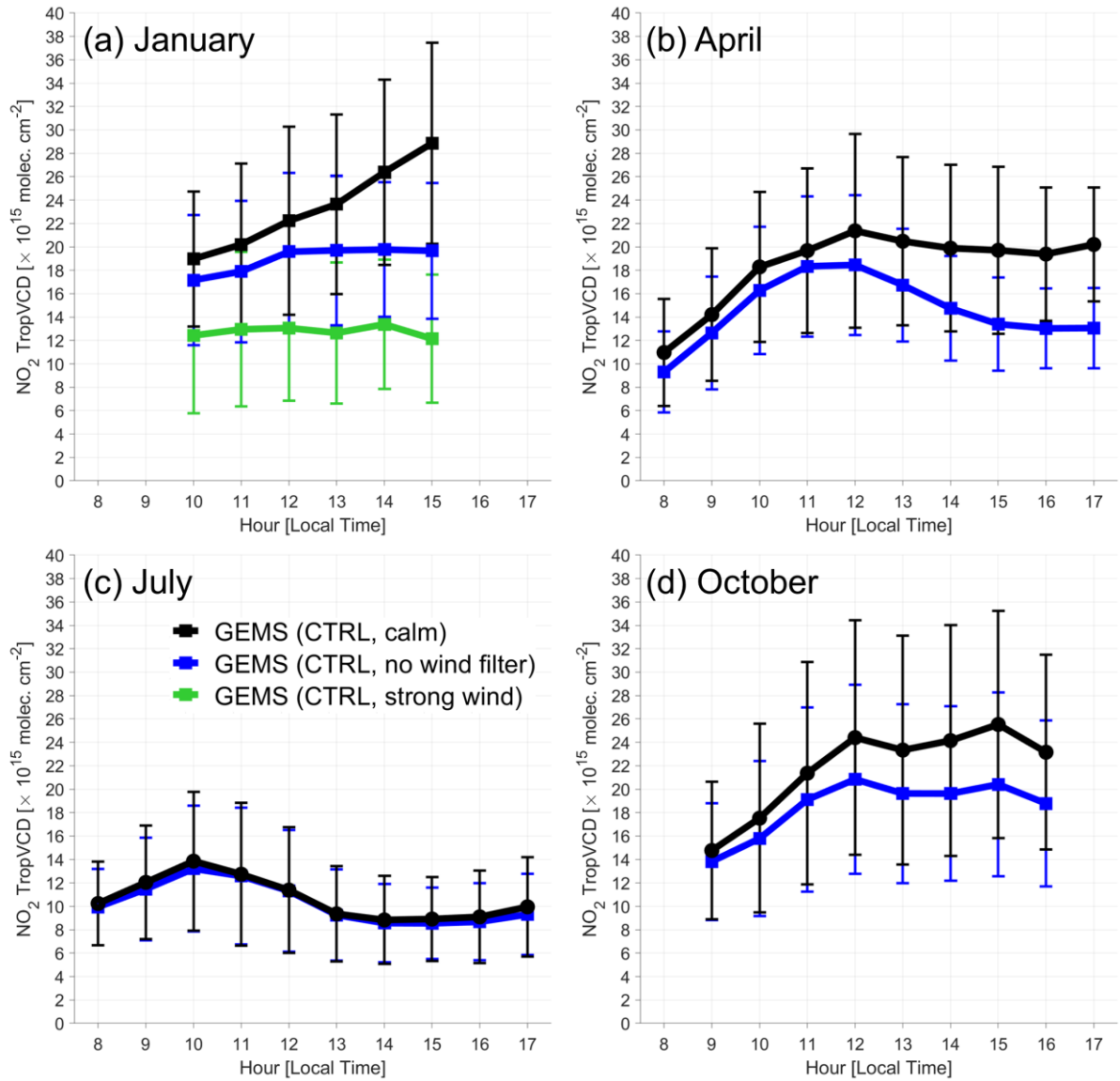




1

2 **Figure 11.** Similar to Figure 9, but for the differences of NO<sub>2</sub> TropVCD between CTRL  
 3 and TM5 run (CTRL – TM5).

4



1

2 **Figure 12.** Diurnal patterns of retrieved NO<sub>2</sub> TropVCDs from the CTRL run in (a)  
 3 January, (b) April, (c) July, and (d) October 2021 over the SMA region. Black lines  
 4 indicate the NO<sub>2</sub> TropVCD values with wind-filtered data; only the scenes with wind  
 5 speed lower than 3m/s are utilized. Blue lines are the averaged values without any wind  
 6 filters. The green line is for case of strong-wind run with the NO<sub>2</sub> TropVCD being  
 7 selected and averaged for wind speeds faster than 5m/s in January.